European Society of Computational Methods in Sciences and Engineering (ESCMSE)

Journal of Numerical Analysis, Industrial and Applied Mathematics (JNAIAM)
vol. 19, no. 3-4, 2026, pp. 1-20
ISSN 1790–8140

Effect of Dual-Permeability Structures on the Thermo-Hydraulic Performance of Metal Foam Porous Media

A. Alrudhan and G. Bognár[1]

Institute of Machine and Product Design,
Faculty of Mechanical Engineering and Informatics,
University of Miskolc,
3515-Egyetemváros, Miskolc, Hungary

Received 7 August, 2025; accepted in revised form 31 October, 2025

Abstract: A computational fluid dynamics investigation of porous metal foam fully filling a horizontal pipe was conducted to optimize the balance between thermal and hydraulic performance. The study examined six different models of aluminium metal foam, which featured both dual and uniform permeability configurations. The dual permeability setup featured porous metal foam arranged in series with uniform dimensions. The pore density of metal foam varies from 10 to 20 PPI and its porosity is 0.9, 0.92, and 0.94. The Darcy-Extend Forchheimer model was used for flow dynamics within the porous region. The local thermal non-equilibrium (LTNE) model was applied within the porous filled region of the pipe to analyze heat transfer characteristics. The results showed that the thermal performance of the dual permeability structure (model 5 and 6) was better than the uniform permeability structure (models 1, 2, 3, and 4). The combination of 10 PPI and 30 PPI in a dual permeability series structure was found to optimize thermal performance, while the combination of 20 PPI and 30 PPI optimized hydraulic performance across all mass flux values. The average wall temperature, average Nusselt number and friction coefficient were also computed to determine the optimal performance.

Keywords: Heat flow, Metal foam, Porous media, Dual permeability

Mathematics Subject Classification: 80A20

PACS: 44.10.+i, 47.56.+r, 44.05.+e

1. Introduction

The transport of heat and fluid through porous media presents significant complexity due to the irregular and spatially varying flow geometry within the structure. This variety often leads researchers to shift focus from the complicated local behaviors to the macroscopic ability of the medium to facilitate energy and fluid transport. Such an approach does not imply that the underlying flow becomes simplified since truly laminar or turbulent flows, in the conventional sense, are absent in porous materials but rather that the overall description of the process is made more tractable [1]. Over the past few decades, metal foams have attracted increasing interest within the research community owing to their exceptional ability to enhance heat transfer. As a result, they have been incorporated into a wide range of thermal systems, including geothermal applications, compact heat exchangers, air-cooled condensers, advanced electronic cooling devices, combustion chambers, and the solidification processes in metal casting [2]. As the demand for more integrated and compact power systems continues to rise, there is an increasing emphasis on developing lightweight and space-efficient heat exchange equipment. Currently, porous media are widely utilized in advanced heat exchanger designs to meet these requirements [3-5]. Open-cell metal foams, in particular, feature a complex network of randomly distributed and irregularly interconnected pores. This unique structure results in a high specific surface area and promotes intense flow disturbances, making metal foams especially attractive for enhancing thermal performance in such systems [6-8]. Studied the convection heat transfer numerically when using porous media filled the heat exchanger, and carried out a study of the effects of

[1] Corresponding author. E-mail: gabriella.v.bognar@uni-miskolc.hu

Nomenclature

A_{sf}	Interfacial surface area (1/m)
C	Constant
C_p	Specific heat (J/kg.K)
C_F	Drag coefficient (1/m)
d_f	Fiber diameter (m)
d_P	Pore diameter (m)
D_{in}	Inner diameter of pipe (m)
D_h	Hydraulic diameter (m)
f	Friction coefficient
$\dot{G}$	Mass flux (kg/m^2.s)
GCI	Grid convergence index
h_{sf}	Interfacial heat transfer coefficient (W/m^2.K)
h_{av}	Average heat transfer coefficient (W/m^2.K)
K	Permeability (m^2)
k_s	Thermal conductivity of solid (W/m.K)
k_f	Thermal conductivity of fluid (W/m.K)
LTNE	Local thermal non-equilibrium model
L	Length of the pipe (m)
Nu_{av}	Average Nusselt number
PPI	Pores per inch
p	Perimeter of the pipe (m)
P	Order of accuracy
Pr	Prandtl number
q_w	Heat flux (W/m^2)
Re_K	Reynolds based on permeability
Re_{df}	Reynolds based on fiber diameter
r	Grid ratio
T	Temperature (K)
$T_{a.w}$	Average wall temperature (K)
T_{av}	Average temperature (K)
S	Grid size
$\boldsymbol{u}$	Intrinsic fluid velocity (m/s)
$\boldsymbol{U}$	Superficial (Darcy) velocity

Greek Symbols

ε	Porosity
ϵ	Relative error
μ_f	Dynamic viscosity of fluid (N.s/m^2)
μ_t	Turbulent viscosity of fluid (N.s/m^2)
ρ_f	Density of fluid (kg/m^3)
ρ_s	Density of solid (kg/m^3)
Δp	Pressure drop (Pa/m)
ϖ	Turbulent specific dissipation rate
k	Turbulent kinetic energy
$\boldsymbol{\upsilon}$	Kinematic viscosity

Subscript

eff	Effective

the Reynolds number, temperature difference between fluid in and fluid out, the results showed the mean Nusselt number enhances with the Re numbers [9]. Investigated the numerical examination of the effect of spatial porosity variation of aluminium metal forms filled in a vertical pipe, the results show that the pressure drop slightly decreases for spatially varied porous media as compared with uniform porosity metal foam [10]. Studied partially filled high porosity metallic foams in a horizontal direction pipe and the effect of heat transfer and pressure drop, the results showed thermal performance factor for a variety of PPI and porosity [11]. This study investigates the effect of spatial permeability variation in aluminium metal foam porous media on heat transfer and pressure drop within a fully filled horizontal tube. Numerical modeling of such porous media becomes essential to avoid the high costs associated with procuring metal-based porous materials and conducting experimental analyses. The volume-averaged technique has proven to be a computationally efficient approach for simulating flow and heat transfer in these media, which often involve complex internal structures [28]. Several experimental, analytical, and numerical studies have been conducted to investigate the hydrodynamic and thermal characteristics of porous media within horizontal and vertical channels. The impact of gradient porosity in metal foams has also been examined by various researchers [29-31].
From the perspective of numerical analysis and applied mathematics, the present work addresses the computational challenges arising from the solution of a nonlinear and strongly coupled system of partial differential equations governing flow and heat transfer in porous media. The Darcy–Extended Forchheimer formulation introduces nonlinear inertial resistance terms that depend quadratically on velocity, while the local thermal non-equilibrium (LTNE) model leads to a two-equation energy system coupled through interfacial heat exchange. This results in a convection–diffusion–reaction system with multiscale features and potential numerical stiffness, especially in the presence of turbulence and spatial variations in permeability. Consequently, the formulation, discretization, and verification of a stable and accurate numerical scheme become central to the study. In this work, a second-order finite-volume framework combined with pressure–velocity coupling and pseudo-transient stabilization is employed, and its performance is rigorously assessed through grid convergence index (GCI) analysis and benchmark validation. These aspects highlight fundamental issues of discretization accuracy, convergence behavior, and numerical stability in solving Darcy–Forchheimer-type equations. Therefore, beyond its engineering relevance, this study contributes to the computational treatment of nonlinear transport problems in porous media and directly aligns with the core objectives of numerical analysis, industrial mathematics, and applied mathematical modeling emphasized by the journal.

2. Geometry and boundary conditions

The tube is fully filled with metal foam porous media, with a length of 1000 mm, an inner diameter of 100 mm, and an outer diameter of 107 mm [11]. The uniform heat flux of 275 W/m^2 is exposed over the wall of the porous media section [11]. The inlet and outlet of non-porous pipe section were adiabatic wall boundary conditions, 1000mm length for each one to ensure fully developed turbulent flow rate at inlet and to prevent the back affects at outlet as shown in Fig. 1. The aluminum foam is fully filled inside the tube with different pore densities (PPI) of 10, 20 and 30 with porosities 0.9, 0.92 and 0.94 based that ranges for best performance of maximum heat transfer and minimum pressure drop [12,13,14]. The flow inside the tube is assumed to be turbulent flow, and Re_K varies from 22 to 153, which depends on the uniform and dual permeability, where the effective permeability K_{eff} is used for multiple permeability models [15]. In order to improve the thermal performance and minimize pressure drop inside a fully filled tube, six different models are considered for the computational domain. The first to fourth models are uniform permeability, and the other two models are dual permeability as shown in Table 1. In model 1, have low PPI 10, porosity 92%, model 2 high PPI 30, low porosity 90%, model 3 high PPI 30, high porosity 94% and model 4 PPI 20, porosity 92%. In the model 5 of dual permeability in series between model 1 and model 2, as for model 6, also dual permeability in series between model 4 and model 3, respectively. A 3-dimensional computational domain is considered. A constant velocity inlet of the duct is defined, while a pressure outlet duct is applied. The interfacial coupling conditions between fluid and porous medium are governed by Eqs.1-11. To ensure physical consistency at the interface between a porous medium and a clear fluid region, continuity of velocity, shear stress, and heat flux must be maintained for both heat and fluid flow, as shown in Table 2 and details of boundary conditions in Table 3 [16]. In ANSYS FLUENT 25, the porous metal foam region and the clear fluid region are modeled as two distinct cell zones. The interfaces between these zones serve as coupling boundaries, enabling interaction between the porous and fluid domains. When employing the Local Thermal Non-Equilibrium (LTNE) model, the solid and fluid phases are treated separately. Within the porous region, the thermal and physical properties of the metallic foam are

specified according to the LTNE framework to accurately capture the heat transfer behavior between the solid matrix and the fluid phase.

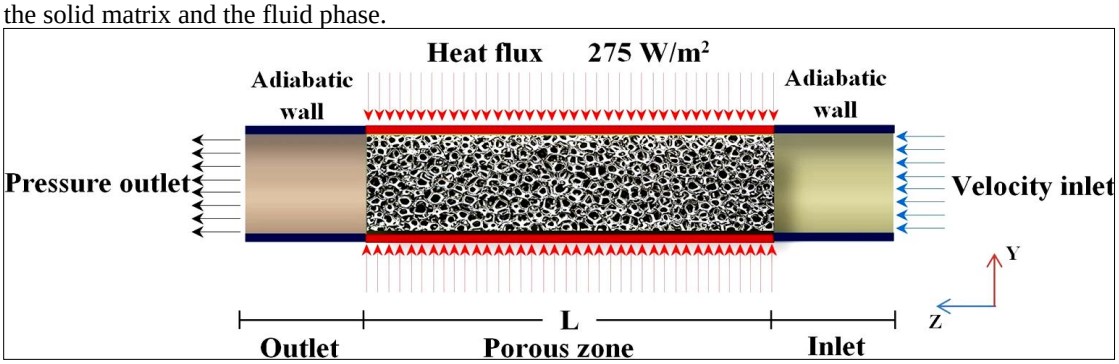

Figure 1: Schematic of the computational domain.

Table 1: Configurations of the models considered

Pattern	Configuration	Permeability (m^2)	Inertial resistance (1/m)
Model 1	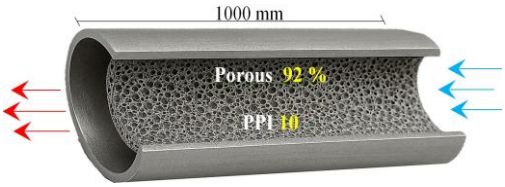	$K = 4.36\times10^{-6}$ Uniform permeably	121.3
Model 2	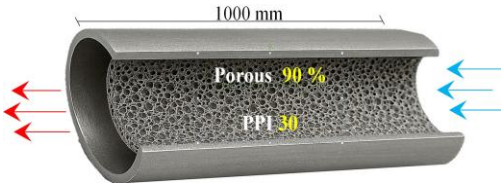	$K = 2.9\times10^{-7}$ Uniform permeably	283
Model 3	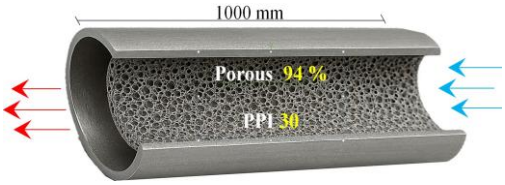	$K = 9.19\times10^{-7}$ Uniform permeably	298.7
Model 4	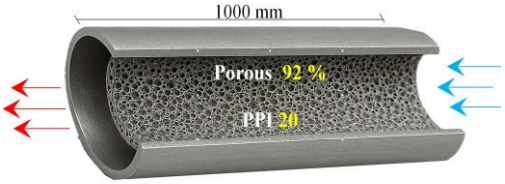	$K = 1.09\times10^{-6}$ Uniform permeably	242.5
Model 5	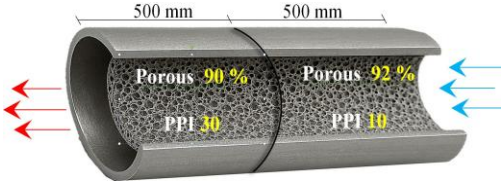	$K_{eff} = 5.43\times10^{-7}$ Dual permeably	121.3 , 283
Model 6	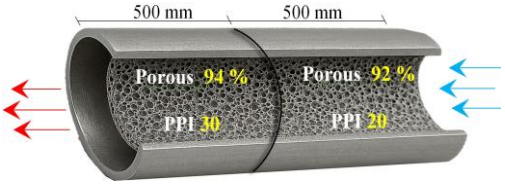	$K_{eff} = 9.97\times10^{-7}$ Dual permeably	242.5 , 298.7

Table 2: Coupling conditions at the porous interface

Property	Condition
Fluid velocity	$u\big\vert_{\ Interface^+} = u\big\vert_{\ Interface^-}$
Shear stress	$\frac{k_f}{\varepsilon}\frac{\partial\langle u\rangle}{\partial x}\big\vert_{\ Interface^+} = k_f\frac{\partial\langle u\rangle}{\partial x}\big\vert_{\ Interface^-}$
Fluid temperature	$T_s\big\vert_{\ Interface^+} = T_f\big\vert_{\ Interface^-}$
Heat flux	$-k_{se}\nabla T_s.\boldsymbol{n} = h_{sf}(T_s - T_f)$ $q = -(k_{fe}\nabla T_f + k_{se}\nabla T_s).\boldsymbol{n}$ $q = -k_f\nabla T_f$ inside porous region

Table 3: Applied boundary conditions for the numerical model

Region	Condition	Description
Inlet Z=0	$w=w_{in}$, $u=v=0$, $T=T_{in}$	Uniform velocity and temperature inlet
Outlet Z=3L	$\frac{\partial u}{\partial y} = \frac{\partial v}{\partial z} = \frac{\partial w}{\partial x} = 0, \frac{\partial T}{\partial z} = 0$	Fully developed outflow
Entry & Exit walls	$x=X$, $y=Y$: $u=v=w=0$, $\frac{\partial T}{\partial x} = \frac{\partial T}{\partial y} = \frac{\partial T}{\partial z} = 0$	No-slip, adiabatic wall
Heated wall	$x=X$, $y=Y$: $u=v=w=0$, $q_w=q''$	*Constant heat flux* $q'' = 275W/m^2$
Interface between wall and metal foam	$q_w = (k_{fe}\nabla T_f + k_{se}\nabla T_s).\boldsymbol{n}\big\vert_{\ Interface}$	Heat flux continuity

2.1. Problem formulation

By using ANSYS FLUENT 25, the numerical computations are examined. The air properties are computed depending on the fluid inlet temperature. The velocity of air varies from 0.6639 m/s to 2.1 m/s [11], meanwhile, the Re_K is calculated based on hydraulic diameter [15], uniform and multiple permeability of duct that varies from 22 to 153, i.e.

$$K_{eff} = L_{total}/\sum_{i=1}^{n}\frac{L_i}{K_i} \tag{1}$$

As a result of the ranges of velocity and Re number, the flow inside the duct is assumed to be turbulent. The two equations k-ω turbulence model is applied [16, 17]. The porous section of the duct is modeled as a homogeneous, isotropic medium. To capture the characteristics of airflow within the porous foam region, the Darcy–Extended Forchheimer model is applied. In this framework, the Darcy–Extended Forchheimer model introduces a source term into the momentum equation to account for flow resistance. Both viscous and inertial losses associated with permeability and the form drag coefficient, respectively, are incorporated into the momentum formulation. The governing equations used to describe the flow in the foam-fully-filled region of the duct are presented below [18].
Conservation of mass for single-phase fluid in a rigid porous medium:

$$\frac{\partial(\varepsilon\rho)}{\partial t} + \nabla.(\rho U) = 0, \tag{2}$$

where $\mathbf{U} = \varepsilon\mathbf{u}$,

$$\frac{\partial(\varepsilon\rho)}{\partial t} + \nabla.(\varepsilon\rho u) = 0.$$

For incompressible flow in a rigid porous medium (ρ=constant, ε=constant)

$$\nabla.U = 0,$$

or equivalently

$$\nabla.(\varepsilon u) = 0. \tag{3}$$

Conservation of momentum

$$\frac{\partial(\varepsilon\rho_f u)}{\partial t} + \nabla.(\varepsilon\rho_f uu) = -\varepsilon\nabla p + \nabla.[\varepsilon\mu(\nabla u + (\nabla u)^T)] + \varepsilon\rho_f g - \frac{\mu}{K}U - \rho_f C_F|U|U. \tag{4}$$

Energy equations in porous LTNE:

i. Fluid phase (convection and conduction)

$$\varepsilon(\rho c_p)_f \frac{\partial T_f}{\partial t} + (\rho c_p)_f U.\nabla T_f = \nabla.(\varepsilon k_f \nabla T_f) + h_{sf} a_{sf}(T_s - T_f). \quad (5)$$

ii. Solid phase (conduction)

$$(1-\varepsilon)(\rho c_p)_s \frac{\partial T_s}{\partial t} = \nabla.\left((1-\varepsilon)k_s \nabla T_s\right) + h_{sf} a_{sf}(T_f - T_s). \quad (6)$$

In the present numerical analysis, heat dispersion within the porous region is considered negligible, owing to the high thermal conductivity of both the metal foam and the working fluid is air [19]. The pressure–velocity coupling is handled using a pseudo-transient scheme to ensure numerical stability and convergence. A second-order discretization scheme is applied to the pressure, momentum, and energy equations to enhance solution accuracy. The convergence criteria are set to 10^{-5} for the continuity and momentum equations, 10^{-3} for the *k-ω* turbulence equations, and 10^{-10} for the energy equation [20, 21, and 22]. The properties of metal foam, such as interfacial area density a_{sf} and interfacial heat transfer coefficient h_{sf} are computed based on Eq. 7 and Eq. 8, respectively [19,23].

Superficial area density:

$$a_{sf} = \frac{3\,\pi d_f\left(1 - e^{-\left(\frac{1-\varepsilon}{0.04}\right)}\right)}{(0.59\,d_p)^2} \quad (7)$$

Interfacial heat transfer coefficient:

$$h_{sf} = \frac{k_f}{d_f} Nu_{df}(1 - e^{-\frac{1-\varepsilon}{0.04}})^{-1}, \quad (8)$$

where

$$Nu_{df} = \begin{cases} 0.76\, Re_{df}^{0.4}\, Pr^{0.37}, & 1 \le Re_{df} \le 40 \\ 0.526\, Re_{df}^{0.5}\, Pr^{0.37}, & 40 \le Re_{df} \le 10^3 \\ 0.26\, Re_{df}^{0.6}\, Pr^{0.37}, & 10^3 \le Re_{df} \le 2\times 10^5 \end{cases}$$

The Reynolds number based on the fiber diameter Re_{df} of the porous medium is computed by:

$$Re_{df} = u\, d_f \left(\frac{1-e^{-\frac{1-\varepsilon}{0.04}}}{\upsilon\varepsilon}\right), \quad (9)$$

where Re_{df}<1 (Creeping Flow),
1< Re_{df} < 10 (Laminar Flow),
10≤ Re_{df}≤40 (Transitional),
Re_{df}>40 (Turbulent Flow).

The following term is the porosity correction factor often used in fibrous media correlations:

$$\frac{1-e^{-\frac{1-\varepsilon}{0.04}}}{\varepsilon}.$$

2.2. Grid independence

A grid independency study is conducted to determine the optimal mesh resolution for the proposed numerical model. A constant heat flux is assumed of 275 W/m^2 which exposed at the wall of the porous media metal foam wall region. An aluminium duct fully filled with porous media of 10 PPI and 92% porosity at Re_K =22 is selected for grid independence. Five different grid sizes of 152,388, 334,212, 510,772, 783,544, and 945,720 are accomplished for this study. The maximum wall temperature (T_{max}) was selected as the monitoring parameter because it is directly related to the thermal performance of the porous medium. To quantitatively assess mesh convergence, Richardson extrapolation theory was applied. The observed discretization error between successive meshes is expressed as:

$$|T_{max2} - T_{max1}| = C\, S^P, \quad (10)$$

where S is the characteristic grid size, C is a constant, and P is the observed order of accuracy.

The representative grid refinement ratio between two consecutive meshes was calculated from

$$r= \frac{h_{coarse}}{h_{medium}} = \sqrt{\frac{N_{medium}}{N_{coares}}},$$

where N denotes the total number of computational cells for the two-dimensional domain. Using three consecutively refined grids (334,212, 510,772, and 783,544); the observed order of convergence was determined from

$$P = \left(\ln\left(\frac{T_{coarse} - T_{medium}}{T_{medium} - T_{fine}}\right) \Big/ \ln(r) \right) \quad (11)$$

The resulting convergence order was found to be approximately p=1.8.
which is also close to the theoretical second-order accuracy expected from the discretization schemes employed in ANSYS Fluent. This agreement confirms that the numerical solution lies within the asymptotic convergence range.
To further quantify the discretization uncertainty, the grid convergence index (GCI) recommended by the ASME procedure was calculated as

$$GCI_{fine} = \frac{1.25\,|\epsilon|}{r^p - 1} \times 100\% \quad (12)$$

where

$$\epsilon = \frac{T_{fine} - T_{medium}}{T_{fine}} \quad (13)$$

ϵ is the relative error between the two finest grids. The calculated GCI value was below 0.05%, indicating negligible discretization uncertainty and demonstrating that further mesh refinement produces an insignificant change in the predicted temperature field.

Table 4: Mesh density and corresponding maximum temperature

Number of grid (elements)	**Maximum temperature (˚C)**
152,388	43.11
334,212	42.99
510,772	42.94
783,544	42.933
945,720	42.922
1,121,670	42.922 *Base line data*

To quantify the discretization error and ensure computational reliability, a grid convergence index (GCI) analysis based on Richardson extrapolation was performed. The observed order of convergence was (p≈1.8), indicating near second-order spatial accuracy. Using the two finest meshes (783,544 and 945,720 elements), the approximate relative error was 0.026%, while the fine-grid GCI was 0.173%. Consequently, the numerical uncertainty associated with the predicted maximum temperature was estimated as $\mp 0.074\%$ °C. Since the discretization uncertainty was below 0.2%, the solution can considered grid-independent and numerically reliable.

2.3. Verification of numerical solutions

To verify the present approach, the predicted temperature distribution and pressure drop of the porous media duct are compared with the numerical study reported by Prakash H. Jadhav et. al. [11]. Aluminium metal foam of 10 PPI and porosity 92% was studied, which is shown in Fig. 2. The temperature distribution at the outlet cross section is compared for three cases: a fully porous pipe, a partially porous [11] pipe and a non-porous pipe. The inlet diameter was 0.1 m, and the air velocity 0.6639 m/s with heat flux 275 W/m^2 for all cases. The simulation results for fully porous configuration demonstrate enhanced uniform temperature as compared with partially porous, while the non-porous pipe exhibits a steep thermal gradient due to limited heat transfer as illustrate in Fig. 3. Regards to pressure drop, the verification of axial pressure drop for three cases: a fully porous pipe configuration, partially porous pipe configuration [11] and non-porous pipe which is shown in Fig. 4. The present study result shows good agreement with Prakash H. Jadhav et. al. data, accurately capturing the

increased significantly with higher porous volume fraction, confirming the models reliability in predicting momentum loss in porous structures. As well, the pressure drop at the outlet area of porous in case of porous configuration does not cause any back pressure, as occurs in the case of the partially porous configuration.

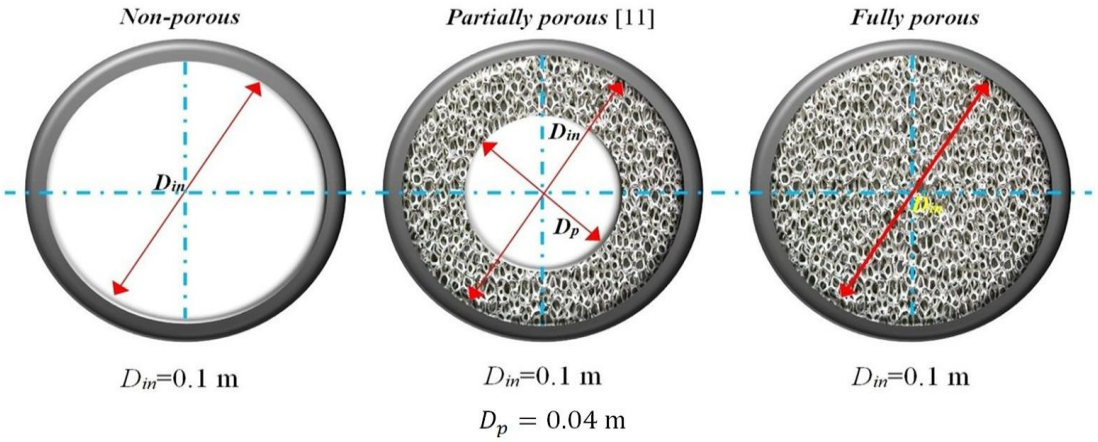

Figure 2: The schematic cross-sections of three different types of porous pipes.

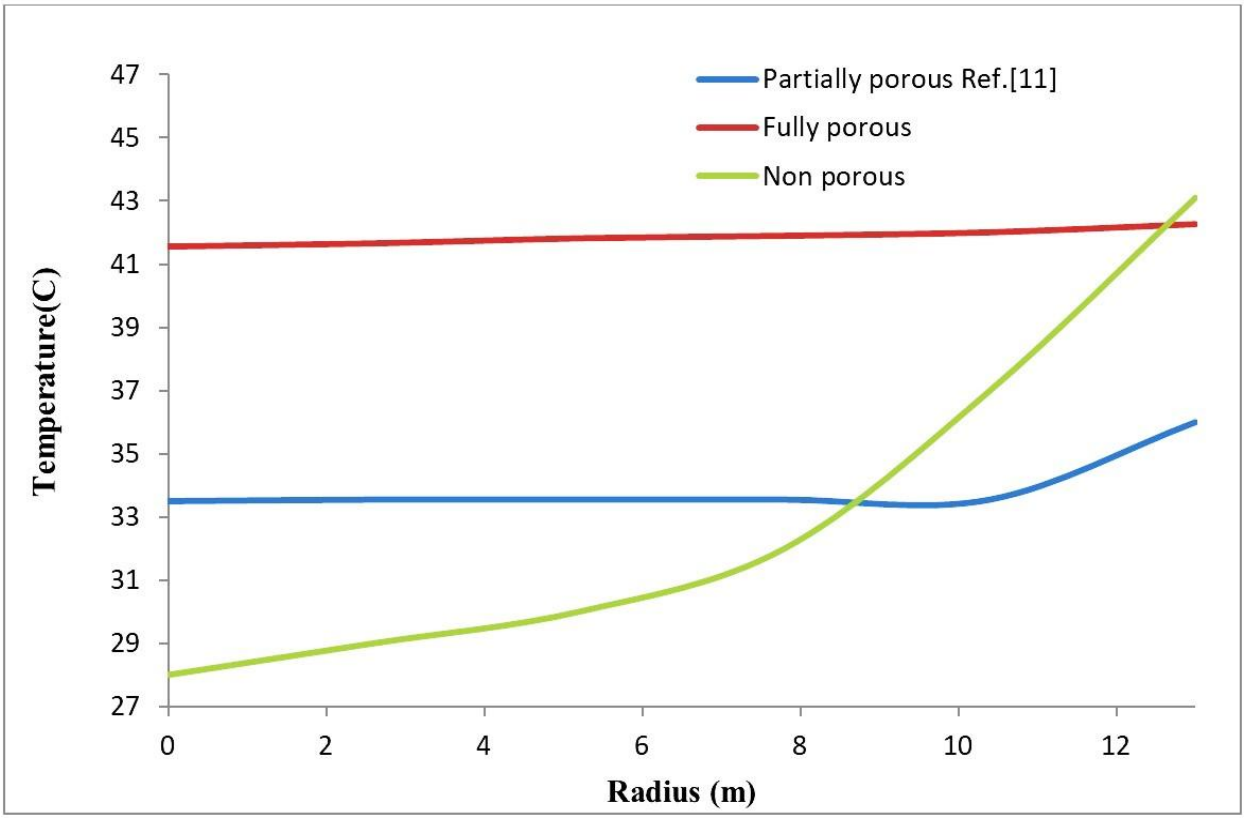

Figure 3: Temperature distribution through the exit area of the porous section.

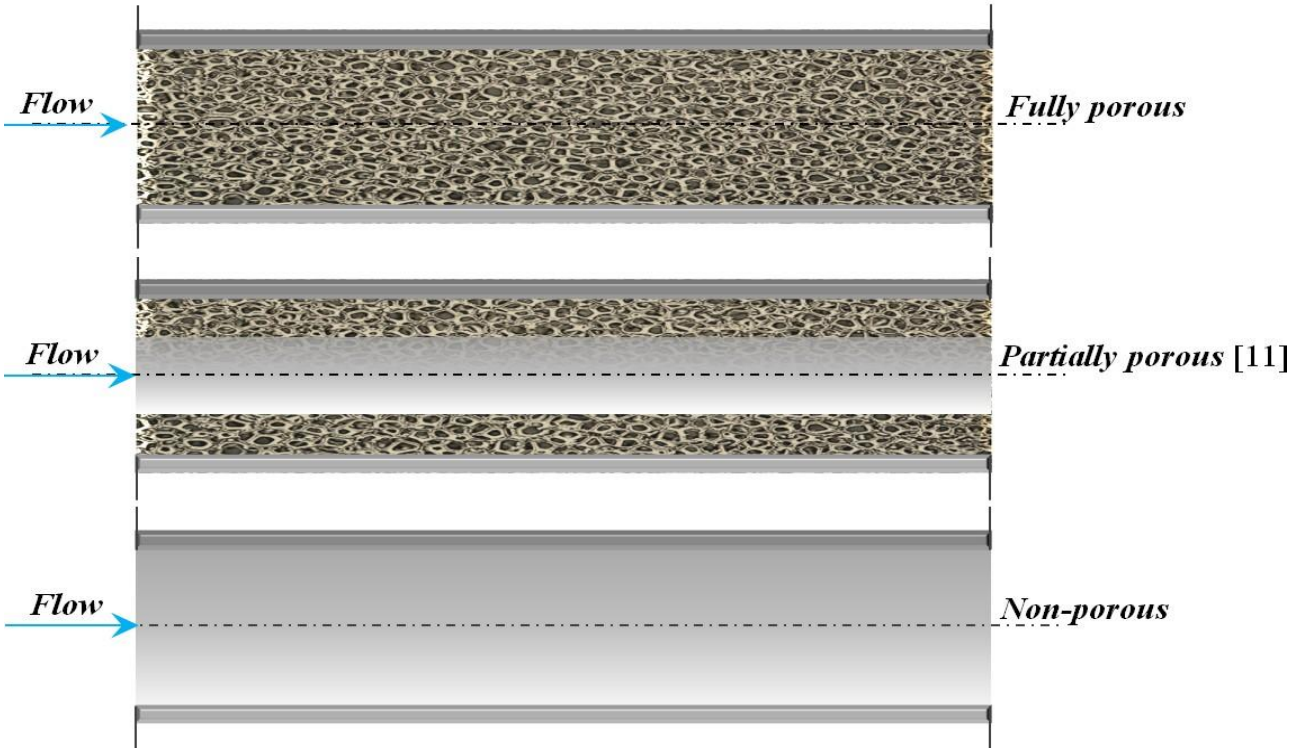

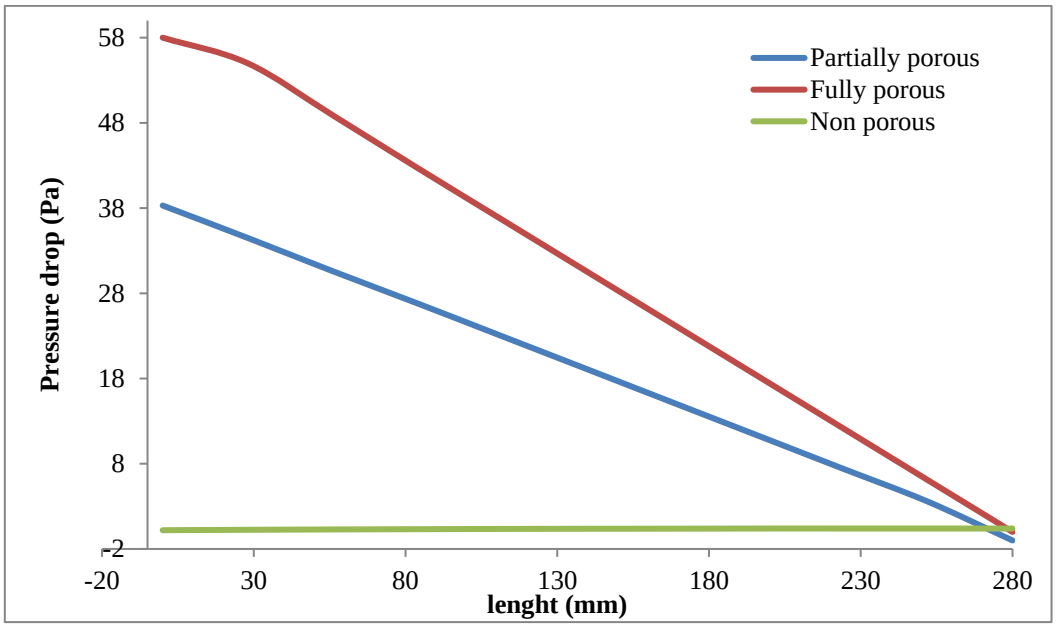

Figure 4: The verification of pressure drop along the porous section.

3. Results and discussion

3.1. Average wall temperature $T_{a.w}$

The contours of average wall temperature for six models under constant heat flux and high air velocity of 2.1m/s, which is shown in Fig. 5. Models 1-4 represent uniform permeability structure with varying pore density and porosity, while models 5 and 6 represent dual permeability structure in series. The results of $T_{a.w}$ show that increased PPI and porosity enhance thermal performance, and the dual permeability configuration model, particularly model 5, yields superior wall temperature reduction due

to optimised conduction-convection coupling within the porous structure. The upstream of model 5 has a low PPI section, which means high resistance will delay heat transfer, but the downstream with high PPI compensates with improved conducting and mixing. As well, the model 6 shows the most favorable wall temperature profile because the temperature gradients enhance local convection heat transfer while managing pressure drop.

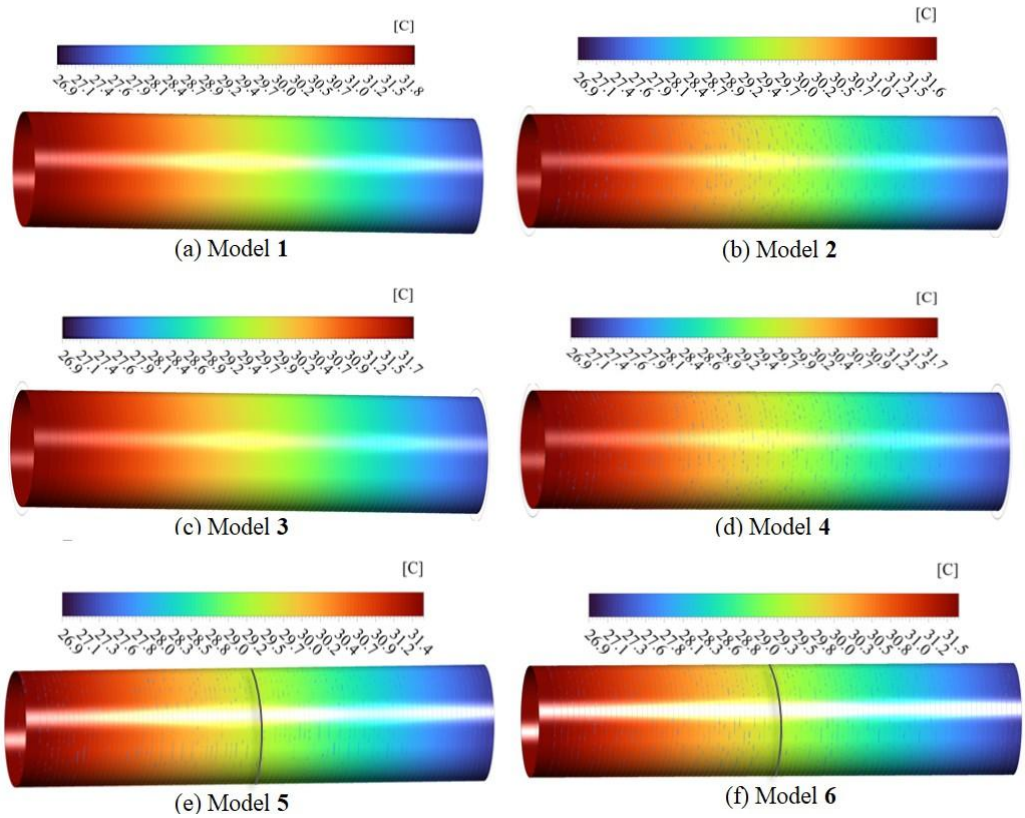

Figure 5: Contours of average wall temperature for configuration models at air velocity 2.1 m/s.

Increasing the fluid velocity in a pipe filled with porous media metal foam leads to a noticeable reduction in wall temperature. This behavior results from enhanced convection heat transfer, reduced boundary layer thickness, and increased thermal dispersion effects to porous structures, as shown in Fig. 6, especially with models 5 and 6, which dramatically decreased average wall temperature, leading to optimized conduction convection coupling. The improvement in heat removal efficiency with velocity is a key design consideration for porous media heat exchangers.
Figure 7 presents the variation of average wall temperature with Reynolds number based on effective permeability Re_K for six porous metal foam models. Models 5 and 6 exhibit superior thermal performance across Re_K range; this is because the impacts of micro-scale structures of metal foam enhance both flow distribution and surface area for heat exchange.

3.2. Temperature distribution

Figure 8 illustrates the air temperature distribution along the length of six models porous media-filled pipes under a constant heat flux of 275 W/m^2 and a low velocity of 0.66 m/s. A clear trend of increasing air temperature along the pipe length is observed for all six different models, which is expected as the fluid absorbs heat from the constant heat flux boundary. The model 2 of high pore density PPI 30 and low porosity 90% generally exhibit a higher temperature rise compared to model 1 with low pore density and high porosity. This is because higher PPI means a smaller pore size and a more meandering path, which enhances the surface area for heat transfer between the solid matrix and the fluid. However, this leads to a greater pressure drop and reduces the fluid mixing, which can impact heat transfer. The most notable observation arises from the dual permeability models 5 and 6. These models combine two different porous media sections in series, leading to improved heat transfer

effects. Model 5, which combines a low pore density and high porosity (10 PPI, 92%) with high PPI and low porosity (30 PPI, 90%), shows a maximum temperature profile as compared with other models. The first section of model 5 provides less resistance to flow and potentially less effective heat transfer, while the second section of high pore density enhances the heat transfer.

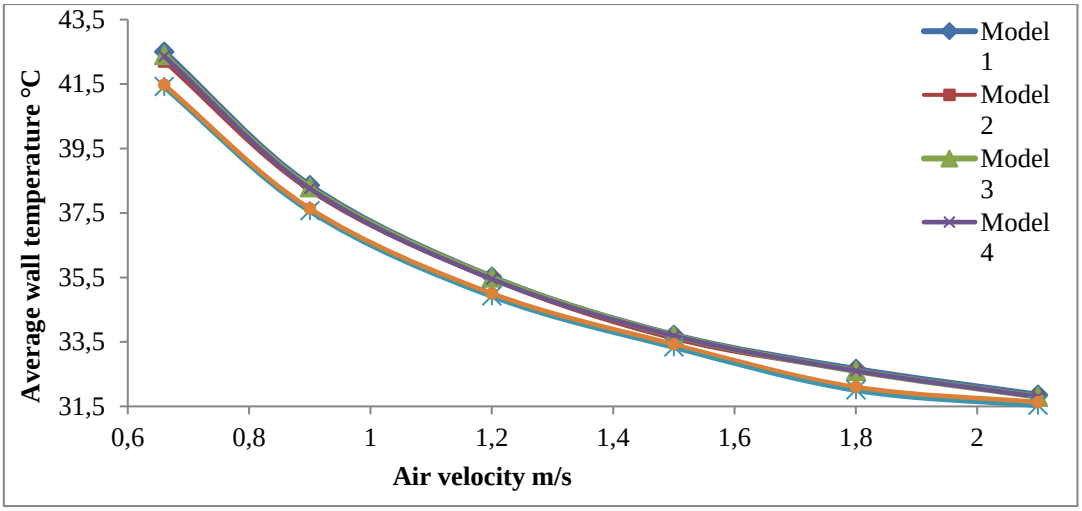

Figure 6: Variation of surface-averaged wall temperature as a function of flow velocity.

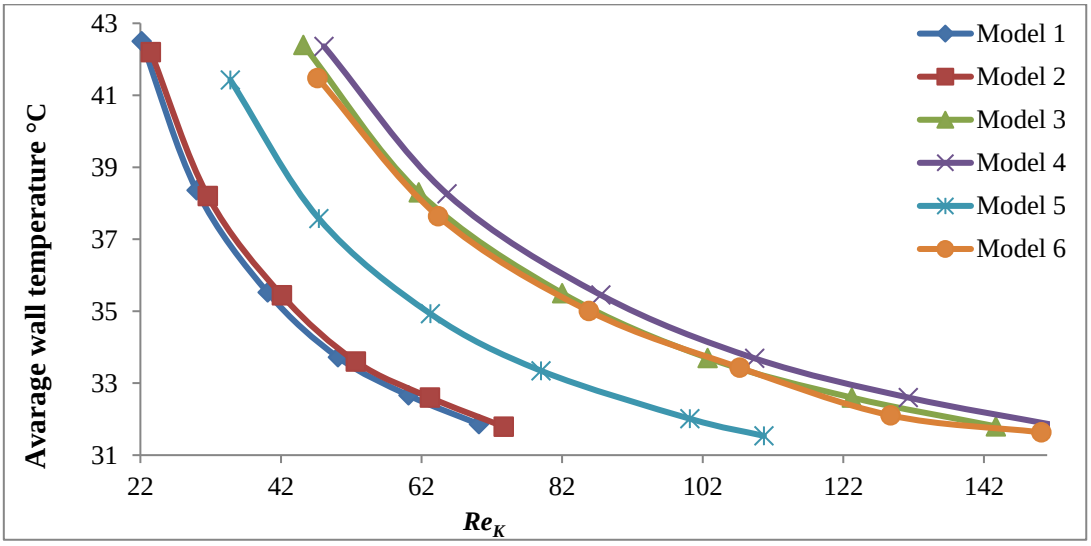

Figure 7: Reynolds number in terms of permeability changes with average wall temperature.

The temperature contours of spatial thermal behavior within a porous media metal foam filled pipe, which is shown in Fig. 9. In a non-porous pipe, the contour refers to classic thermal boundary layer development. A thin layer of higher-temperature fluid is confined to the wall, while the center core of the flow remains at a low temperature. In contrast, the porous media models have a much more uniform temperature distribution across the pipe cross-section. Model 1, due to the effectiveness of heat transfer, results in a high degree of temperature. Model 2, with high pore density and low porosity, presents a slightly more uniform and overall higher temperature profile at exit. Models 3 and 4 show intermediate temperature distributions, consistent with intermediate pore density and porosity. Models 5 and of dual permeability structure explain a unique ability to impact the thermal field. Model 5 shows the clear transition. The first section, with low pore density and high porosity, has a low temperature profile. At the interface, the air enters the higher PPI region, where enhanced surface area and increased flow mixing lead to more effective heat transfer and more rapid temperature enhancement. Model 6 has a similar effect, but with a different initial condition. The thermal performance of the first section is good due to its pore density matrix 20 PPI. The transition to a pore density 30 PPI further

accelerates heat transfer. So the dual permeability configurations highlight the powerful design strategy to optimize the thermal performance along the length of the pipe by strategically arranging different porous media metal foam, to meet specific heat transfer requirements.

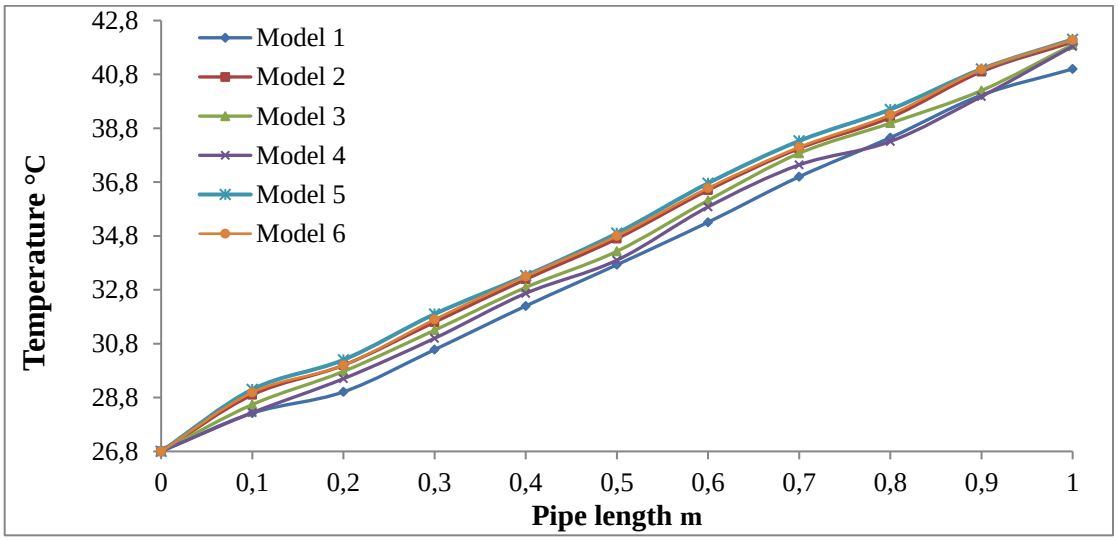

Figure 8: Temperature distribution through porous media pipe section.

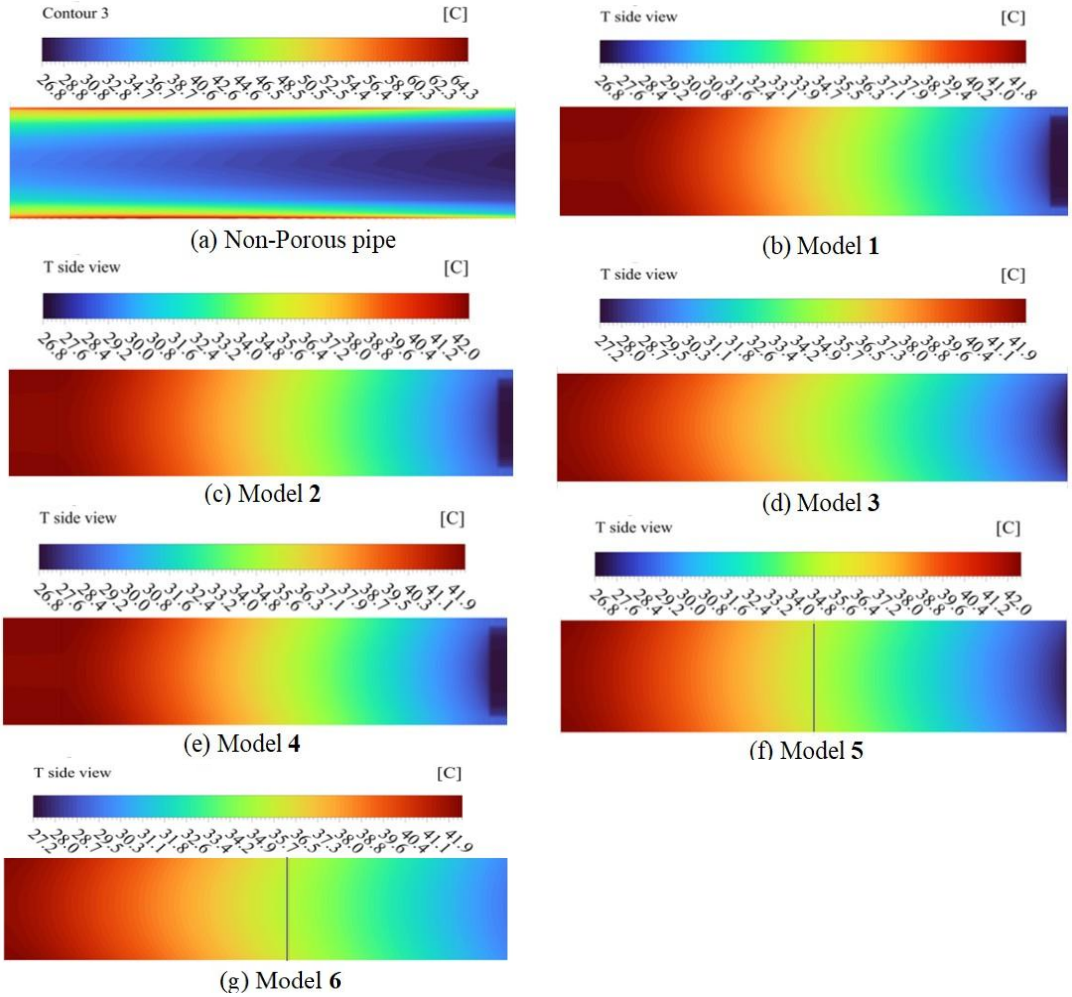

Figure 9: Comparison of temperature contours for porous and clear pipe models at an air velocity 0.66 m/s.

Fig. 10 refers to a parabolic temperature profile shape for a pipe filled with porous media metal foam, which indicates a fully thermally developed condition. The porous media is a composite of a solid

matrix and a fluid. The solid has a much higher thermal conductivity than the fluid. This allows heat to be rapidly conducted from the heated pipe wall into the porous matrix and then disappears throughout the entire volume. This exceeds the low convection heat transfer mechanism of a non-porous pipe, effectively increasing the effective thermal conductivity of the system and leading to more uniform temperature distribution.

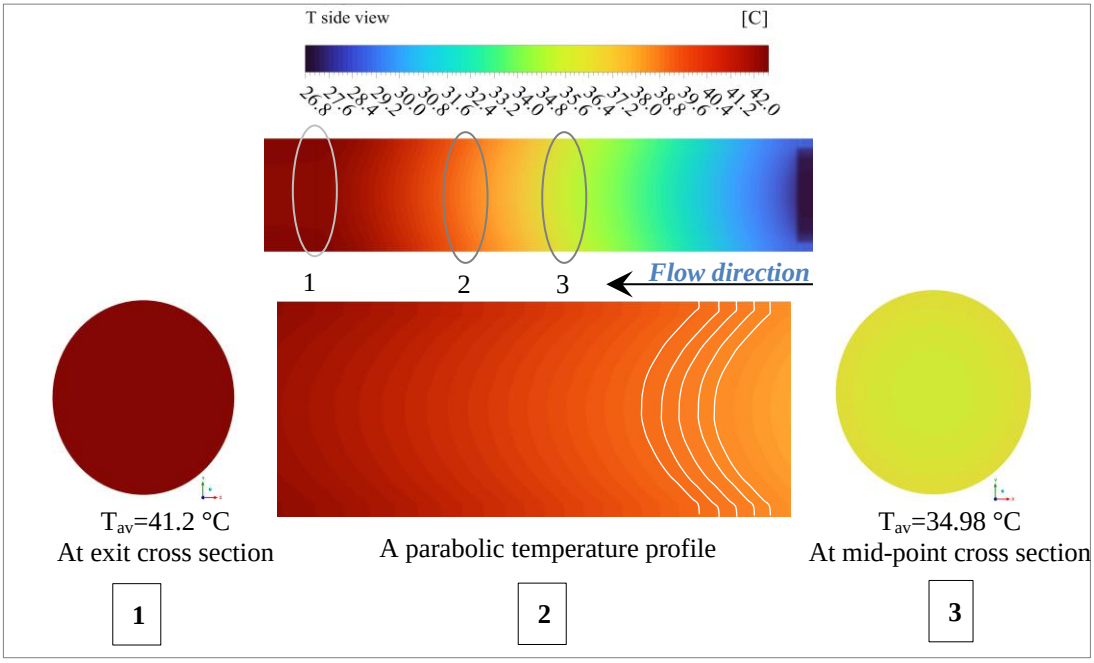

Figure 10: Thermally fully developed region and local average temperature of porous media section

3.3. Convection heat transfer coefficient h_{av}

The average forced coefficient h_{av} is calculated by using Eq. 14.

$$h_{av} = {\Sigma_1^N h_i}/{N} \ . \tag{14}$$

The local forced convection coefficient h_i is computed by using Eq.15.

$$h_i = {q_w}/{T_{wi} - T_{fi}}, \tag{15}$$

where T_{wi} and T_{fi} are the wall and fluid temperature for the given point, respectively.

Figure 11 shows the variation of convection heat transfer coefficient h with mass flux for six models of porous media, metal foam and non-porous pipe under constant heat flux. It's observed that at high flow rate there are enhance of convection effect and a reduction in thermal boundary layer thickness. The models 5 and 6 (dual permeability) consistently outperform single-permeability cases, particularly at higher mass flux values, due to improved flow mixing and increased surface area for exchanging heat. These findings highlight the effectiveness of dual-permeability porous structures in promoting superior thermal performance within fully filled metal foam channels. In the same way, Model 5 used 90% porosity, which means more metal content and leads to high effective thermal conductivity of the porous matrix and better solid conduction through foam structure, which enhances overall heat transfer as compared with model 6 with porosity 94%. The percentage increase in h_{av} for model 5 is 14% as compared with model 1 at mass flux 2 kg/m^2.s. Obviously, the difference in heat transfer coefficient between non-porous and porous pipes for all values of mass flux is due to the increased surface area, disruption of the thermal boundary layer, and enhanced turbulence. The combination of pore density of (PPI 10) with dense surface area (PPI 30) creates an efficient bulk flow and fine heat exchange.

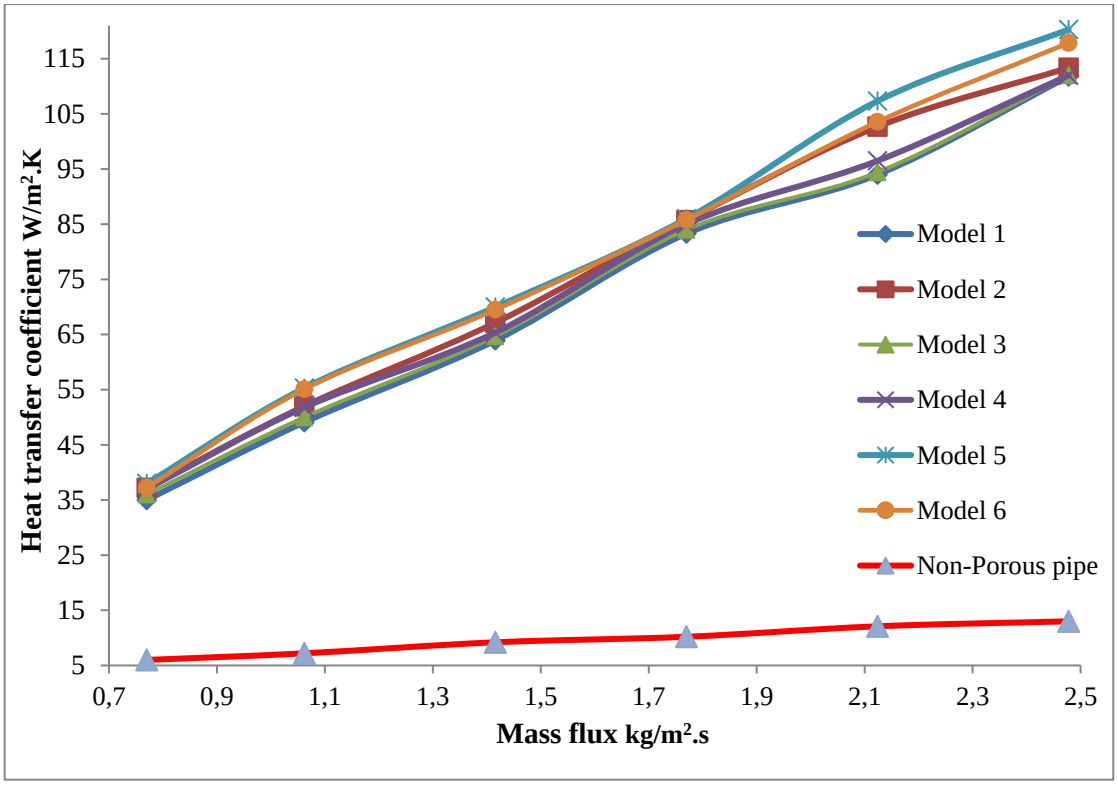

Figure 11: Variation of heat transfer coefficient as a function of mass flux.

3.4. Average Nusselt number Nu_{av}

The mean Nusselt number is computed by Eq.16.

$$Nu_{av} = {}^{h_{av} \cdot D_h}/_{k_{air}}. \tag{16}$$

The hydraulic diameter of the pipe is evaluated by Eq. 17.

$$D_h = {}^{4A_c}/_{p}. \tag{17}$$

Figure 12 explored the average Nusselt number Nu_{av} increased significantly with mass flux across all six metal foam models. This trend is expected, as a higher mass flux leads to increase Reynolds number, promoting thinner thermal boundary layers and stronger convection heat transport with a porous medium. The model 5 consistently achieves the highest Nu values across all mass flux levels. This superior performance is attributed to its dual permeability structure, which combines a PPI 10, porosity 92 % macro foam with a PPI 30, porosity 90 % micro foam. The large pores at pores density PPI 10 make for easy airflow and low pressure drop, while the smaller pores of a pore density PPI 30 offer an increase in surface area for heat transfer. The result is a structure that simultaneously supports effective fluid motion and intense thermal interactions between the solid and fluid phases. Model 6, which also employs a dual permeability structure, shows improved performance over the single permeability models but consistently falls short of model 5. The slightly higher porosity 94 % in model 6 fine foam region, reduces solid material content and thus lowers the effective thermal conductivity and surface area for heat exchange. Furthermore, the intermediate pore size of PPI 20 offers a compromise between permeability and turbulence. The performance of dual permeability confirms the thermo-hydraulic advantage of combining macro-scale flow with micro heat exchange areas. In contrast, the uniform single permeability models 1-4 show progressively low Nu values. Models 2 and 3 benefit from a fine pore structure that increases the surface area, though at the cost of higher flow resistance. Models 1 and 4 allow high fluid flow but low contact area for heat transfer, leading to low Nu_{av}.

The Nu_{av} comparison of the present work with Prakash H. et. al [11] for a range of pore densities PPI and porosities, as shown in Table 5. For the same type of metal foam of aluminium, fluid velocity o.66

m/s and heat flux of 275 W/m^2, the percentage enhancement is 70 % and 66.6 % of Nu_{av} compared with Prakash H. et. al [11]. This enhancement is due to the dual permeability structure, which provides a superior thermal performance. The large pores at low PPI make high mixing airflow and low pressure drop, while the high PPI leads to increasing in surface area of heat transfer. That combination will increase the heat dissipation rate.

Table 5: Nusselt numbers enhancement analysis.

Present work		***Nu*$_{av}$**	**Prakash H. et. al [11]**		***Nu*$_{av}$**	**Enhancement %**
(10 PPI, ε 92 %) + (30 PPI, ε 90 %)	Dual permeability	146.15	20 PPI, ε 90 %	Uniform permeability	86	70
(20 PPI, ε 92 %) + (30 PPI, ε 94 %)	Dual permeability	143.3	30 PPI, ε 92 %	Uniform permeability	86	66.6

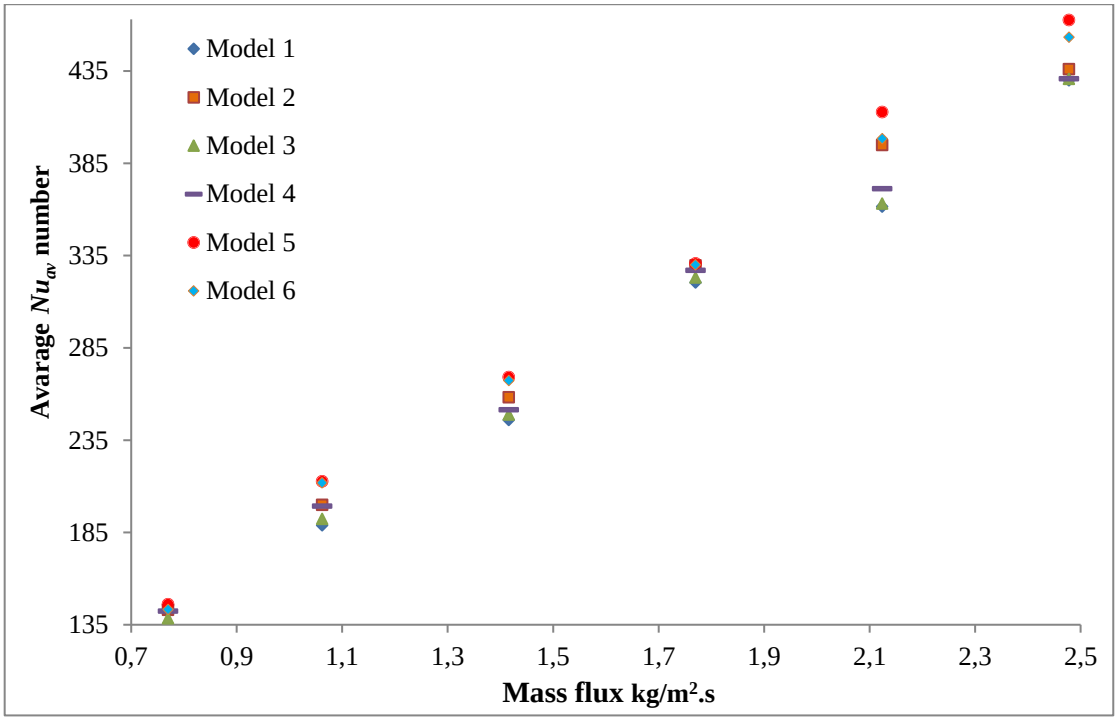

Figure 12: Variation of Nu as a function of mass flux.

3.5. Pressure drop

Figure 13 illustrates the relationship between the pressure drop per unit length and mass flux for the six models of porous media. The comparison of pressure drop between non-porous and porous pipes clearly shows that lower permeability of the porous region leads to greater flow resistance, resulting in a higher pressure drop. This relationship is governed by the Darcy – Forchheimer equation, where the pressure drop is a function of both viscous and inertial effects. The non-linear increase in pressure drop at higher mass fluxes indicates that inertial effects like flow separation and localized turbulence at the interface of solid – fluid, become increasingly dominant over viscous forces. Model 1 shows the lowest pressure drop across all mass fluxes due to low PPI, which means large pores and leads to minimal resistance of fluid flow. Model 2 represents the highest pressure drop. The high pore density and low porosity create a much denser and more mixed fluid, leading to increased viscous and inertial resistance. The finer pore structure enhances the surface area for heat transfer but comes with losses in terms of pumping power. The effect of porosity is highlighted by comparing model 2 with model 3. In spite of having the same pore density 30 PPI, model 3 has higher porosity, providing more void space, which reduces the flow resistance and results in a low pressure drop compared with model 2. Model 4 represents an intermediate case with its pressure drop curve plotting between the low resistance of model 1 and the high resistance of model 2, as expected from the values of pore density.
Dual permeability models of models 5 and 6 show pressure drop characteristics that are a function of their composite structure. Their curves are plotted between the uniform permeability models, reflecting

the combined flow resistance of their two sections in series. The dual permeability structure proves a design strategy to balance thermal performance and hydraulic performance.
The pressure drop contours as shown in Fig. 14 represents the hydraulic resistance imposed by the porous media on the fluid flow. The non-porous pipe refers a minimal pressure drop. The pressure drop due to viscous friction at air velocity 0f 0.66 m/s is negligible. On other hand, the porous media models all show a substantial pressure drop, model 1 which has the lowest flow resistance through porous media. Model 2 has a highest flow resistance due to its higher pore density and low porosity, leads to significant pressure drop. While, the dual permeability structure model 6 shows a fascinating localized control of flow resistance. The first section of dual permeability creates a moderate pressure gradient. The second section has 30 PPI which leads to steeper gradient.

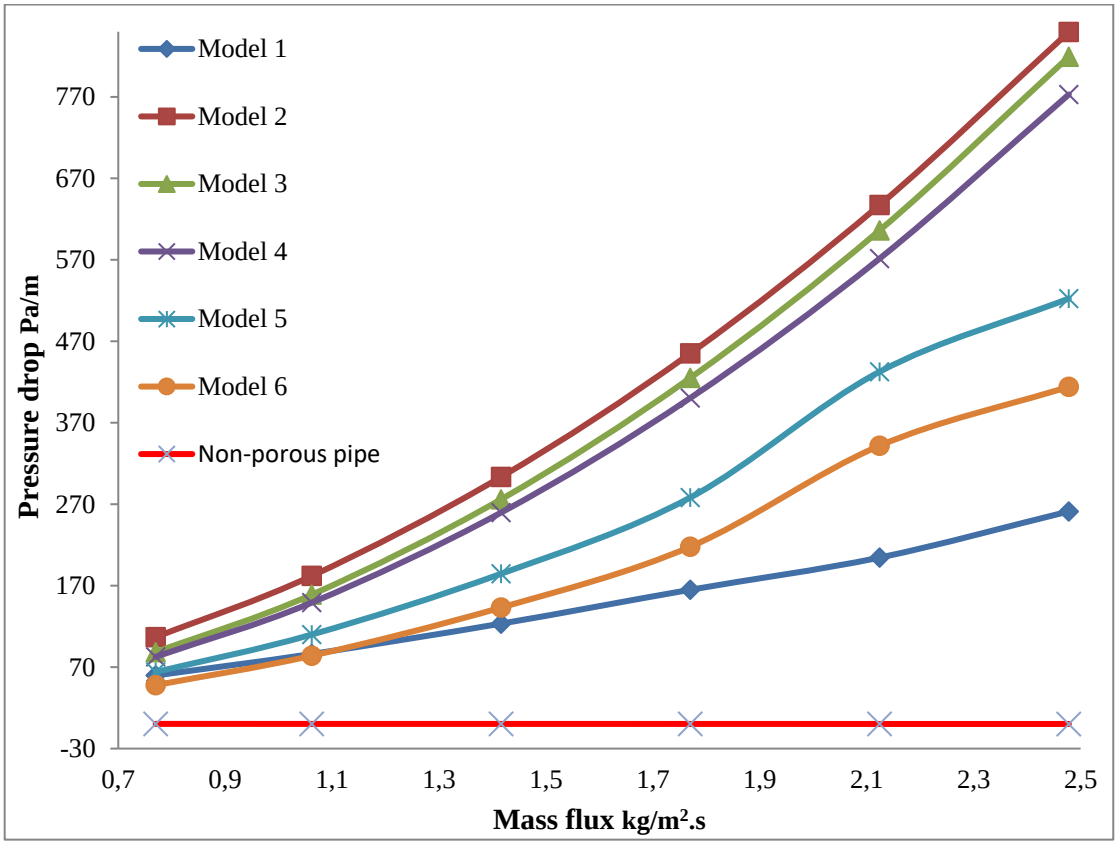

Figure 13: Pressure drop variation with mass flux.

3.6. Friction coefficient

The friction coefficient in a pipe filled with metal foam is computed by Eq.18.

$$f = \frac{2\,\rho_f\,\Delta p\,D_h}{u^2\,L}. \tag{17}$$

Variation of the friction coefficient with mass flux for different porous media models, which is shown in Fig. 15. The friction coefficient, as expected, generally decreases with increasing mass flux due to the dominance of inertial effects over viscous resistance at higher flow rate. However, this curve changes depending on the porous structures and material configuration. Model 1 has a low friction coefficient because low PPI and relatively high porosity result in minimal flow resistance, allowing air to pass with reduced drag. In contrast, model 2 has the highest friction coefficient. The high PPI and lower porosity lead to restricting the air, increasing both viscous and inertial resistance. Models 5 and 6 of dual permeability show moderate friction losses, reinforcing the concept that a dual permeability structure can optimize pressure drop without excessive drag seen in uniformly porous media. Noted, models of dual permeability have a local increase in the friction coefficient around mass flux 2.1 kg/m^2.s. This could be because of the shear or pressure redistribution at the dual permeability interface or due to local flow instabilities or enhanced inertial losses.

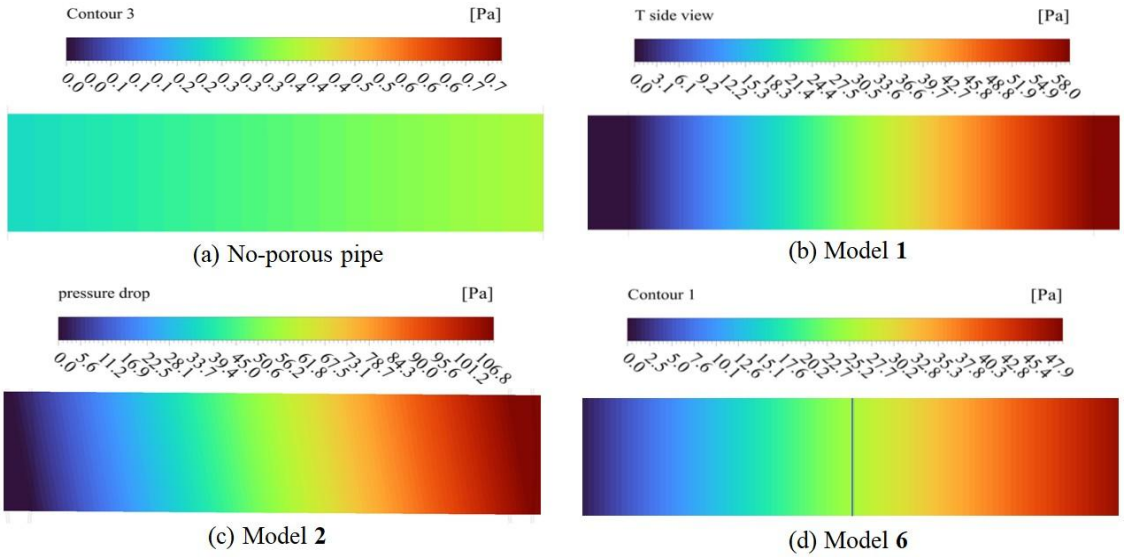

Figure 14: Shows maximum and minimum Pressure drop contours at air velocity 0.66m/s.

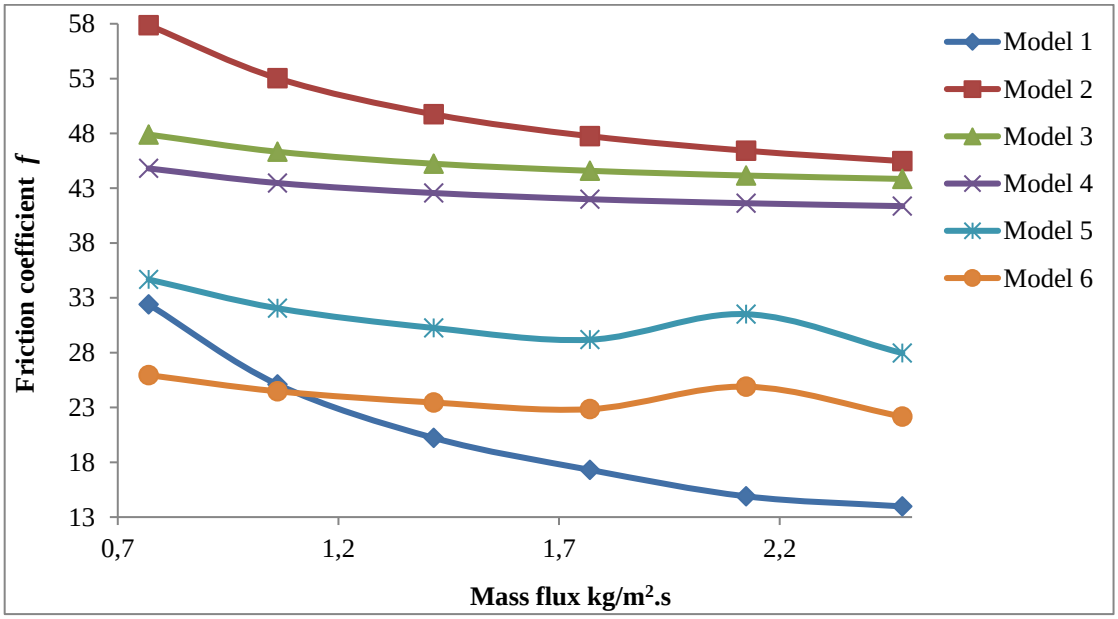

Figure 15: Shows of variation of friction coefficient with mass flux.

4. Conclusion

The present work investigates the mathematical foundation underlying the numerical solution of coupled nonlinear partial differential equations governing transport phenomena in porous media foam. The flow field is described through the Darcy-Extended Forchheimer formulation, which introduces nonlinear inertial resistance terms into the momentum equations. These nonlinear source terms are strongly coupled with energy equations through a temperature–dependent transport mechanism, local thermal non-equilibrium adopted for a porous medium. Consequently, the resulting mathematical model consisted of a system of coupled convection-diffusion-reaction equations whose accurate numerical solution requires careful spatial discretization and iterative linearization.

Therefore, beyond its engineering application, the present work contributes to the computational investigation of nonlinear transport equations in porous media and shows the practical implementation, convergence behavior, and numerical verification of finite-volume discretization for Darcy-Extended Forchheimer flow with LTNE heat transfer. These aspects place the study within the broader scope of

numerical analysis, computational mathematics, industrial mathematics, and applied mathematics modeling.

Three–dimensional numerical simulations were conducted to investigate the impact of dual-permeability porous-media metal foam fully filling a horizontal pipe (0.1 m in diameter, 1 m in length, and 0.07m thickness). The study involved six different models comparing uniform and dual - permeability configurations, with variations in PPI (pores per inch) and porosity for aluminium metal foam. The simulations focused on turbulent forced convection heat transfer, covering a mass flux range from 0.77 to 2.5 kg/m2.s.

Based on the current investigation, the key findings are summarized below:

1. Dual-permeability configurations significantly optimize the temperature distribution and thermal performance in heat exchanger applications.
2. Model 5 enhances the heat transfer coefficient due to improved flow mixing, higher metal content, and an increased surface area for effective heat exchange.
3. The macro foam (10 PPI, 92% ε) for easy airflow and low pressure drop, combined with micro foam (30 PPI, 90% ε) that provides a large surface area for intense thermal, represents an effective combination. This leads to achieving the highest average Nusselt number Nu_{av} across all mass flux levels. Consequently, model 5 has an increase of 14.2 % and 70 % in average Nusselt number compared with model 1 (current study) and partially filled porous media Prakash H. et. al [11], respectively.
4. For a highly effective balance of thermal and hydraulic performance, dual-permeability models 5 and 6 are used. They show moderate pressure drop, positioned between the low resistance of uniform large pore models and the high resistance of fine pore models.
5. The friction coefficient decreases as mass flux increases, dominated by inertial effects at higher flow rates. The dual permeability models 5 and 6 show moderate friction losses. This confirms that their design successfully minimize flow resistance, avoiding the high drag seen in uniformly permeable structure models.

Acknowledgments

The authors gratefully acknowledge the support and resources provided by the Institute of Machine and Product Design. Special thanks to the faculty of mechanical engineering and informatics, University of Miskolc.

References

[1] Bejan, A. *Convection Heat Transfer*, 4th Edition, Wiley, 2013.

[2] Zhao, C.Y. Review on thermal transport in high porosity cellular metal foams with open cells, *International Journal of Heat and Mass Transfer*, 55(13–14) (2012), 3618–3632.

[3] Miao, L., Wang, Y., Kavtaradze, R., Liu, S., Zhang, S. Experimental and numerical analyses of thermal-hydraulic characteristics of aluminium flying-wing fins, *Applied Thermal Engineering*, 203 (2022), 117928.

[4] Wang, C.-C., Chen, K.-Y., Liaw, J.-S., Tseng, C.-Y. An experimental study of the airside performance of fin-and-tube heat exchangers having plain, louver, and semi dimple vortex generator configuration, *International Journal of Heat and Mass Transfer*, 80 (2015), 281–287.

[5] Okbaz, A., Pınarbaşı, A., Olcay, A.B. Experimental investigation of effect of different tube row-numbers, fin pitches and operating conditions on thermal and hydraulic performances of louvered and wavy finned heat exchangers, *International Journal of Thermal Sciences*, 151 (2020), 106256.

[6] Zhao, C.Y. Review on thermal transport in high porosity cellular metal foams with open cells, *International Journal of Heat and Mass Transfer*, 55 (2012), 3618–3632.

[7] Andreozzi, A., Bianco, N., Iasiello, M., Naso, V. Natural convection in a vertical channel with open-cell foams, *Journal of Physics: Conference Series*, 1599 (2020), 012013.

[8] Ali, S., Ihsan, Y. Investigation of forced convection boiling heat transfer for R-134a flow in a vertical tube filled by metal foam, *International Journal of Mechanical & Mechatronics Engineering (IJMME-IJENS)*, 19(3) (2019).

[9] Milani Shirvan, K., et al. Heat transfer and sensitivity analysis in a double pipe heat exchanger filled with porous medium, *International Journal of Thermal Sciences*, 121 (2017), 124–137.

[10] Kiran Kumar, K., et al. Effect of spatial porosity of metal foams on heat transfer filled in a vertical channel, *Materials Today: Proceedings*, 51 (2022), 1539–1547.

[11] Jadhav, P.H., et al. Performance evaluation of partially filled high porosity metal foam configurations in a pipe, *Applied Thermal Engineering*, 194 (2021), 117081.

[12] Boomsma, K., Poulikakos, D. On the effective thermal conductivity of a three-dimensionally structured fluid-saturated metal foam, *International Journal of Heat and Mass Transfer*, 44 (2001), 827–836.

[13] Dukhan, N. Metal Foams: Fundamentals and Applications, *DE Stech Publications*, 2012.

[14] Bhattacharya, A., Calmidi, V.V., Mahajan, R.L. Thermophysical properties of high porosity metal foams, *International Journal of Heat and Mass Transfer*, 45 (2002), 1017–1031.

[15] Nield, D.A., Bejan, A. *Convection in Porous Media*, 5th Edition, Springer, 2017.

[16] Xu, Z.G., Gong, Q. Numerical investigation on forced convection of tubes partially filled with composite metal foams under local thermal non-equilibrium condition, *International Journal of Thermal Sciences*, 133 (2018), 1–12.

[17] ANSYS Fluent. ANSYS Fluent 19.2, Help System, User's Guide/Theory Guide, ANSYS Inc., Canonsburg, PA, 2019.

[18] Huang, Z.F., Nakayama, A., Yang, K., Yang, C., Liu, W. Enhancing heat transfer in the core flow by using porous medium insert in a tube, *International Journal of Heat and Mass Transfer*, 53 (2010), 1164–1174.

[19] Calmidi, V.V., Mahajan, R.L. Forced convection in high porosity metal foams, *Journal of Heat Transfer*, 122 (2000), 557–565.

[20] Jadhav, P.H., Nagarajan, G., Perumal, D.A. Conjugate heat transfer study comprising the effect of thermal conductivity and irreversibility in a pipe filled with metallic foams, *Heat and Mass Transfer*, 56 (2020), 1985–1997.

[21] Kotresha, B., Gnanasekaran, N. Investigation of mixed convection heat transfer through metal foams partially filled in a vertical channel by using computational fluid dynamics, *Journal of Heat Transfer*, 140 (2018), 072601.

[22] Jadhav, P.H., Gnanasekaran, N., Perumal, D.A. Numerical consideration of LTNE and Darcy–Extended Forchheimer models for the analysis of forced convection in a horizontal pipe in the presence of metal foam, *Journal of Heat Transfer*, 143 (2021), 072602.

[23] Zukauskas, A.A. *Convective heat transfer in cross-flow*, in: Handbook of Single-Phase Convective Heat Transfer, S. Kakac, R.K. Shah, W. Aung (Eds.), Wiley, New York, NY, 1987, pp. 4.1–4.57.

[24] Blazek, J. *Computational Fluid Dynamics: Principles and Applications*, 3rd Edition, Elsevier, 2015.

[25] ASME V&V 20 Standard. *Standard for Verification and Validation in Computational Fluid Dynamics and Heat Transfer*, ASME, 2009.

[26] Duan, X., Pei, J., Chen, X., Wang, Y., Ding, C. Enhanced heat transfer in sandwich heat transfer unit with metal foam: A numerical investigation, *Applied Thermal Engineering*, 256 (2024), 124144.

[27] Ali, S.A., Hussain, I.Y. Experimental investigation of convective boiling heat transfer for R-134a flow in metal foam filled vertical tube, *Journal of Mechanics of Continua and Mathematical Sciences*, 14(6) (2019), 168–189.

[28] Calmidi, V.V., Mahajan, R.L. Forced convection in high porosity metal foams, *Journal of Heat Transfer*, 122(3) (2000), 557–565.

[29] Venkateshwar, K., Tasnim, S.H., Simha, H., Mahmud, S. Effect of spatially varying morphologies of metal foams on phase change process, *Thermal Science and Engineering Progress*, 19 (2020), 100667.

[30] Yang, J., Yang, L., Xu, C., Du, X. Numerical analysis on thermal behavior of solid–liquid phase change within copper foam with varying porosity, *International Journal of Heat and Mass Transfer*, 84 (2015), 1008–1018.

[31] Wang, Z., Wu, J., Lei, D., Liu, H., Li, J., Wu, Z. Experimental study on latent thermal energy storage system with gradient porosity copper foam for mid-temperature solar energy application, *Applied Energy*, 261 (2020), 114472.